Design optimization of the plastic scintillators with WLS-fibers and SiPM readouts in the top veto tracker of the JUNO-TAO experiment[*]

Guang Luo,[1] Y.K.Hor,[1, †] Peizhi Lu,[1] Zhimin Wang,[2, 3, ‡] Ruhui Li,[2] Min Li,[2, 3] Yichen Li,[2, 3]
Liang Zhan,[2, 3] Wei Wang,[1, 4, §] Yuehuan Wei,[4] Yu Chen,[1] Xiang Xiao,[1] and Fengpeng An[1]

[1]*School of Physics, Sun Yat-sen University, Guangzhou 510275, China*
[2]*Institute of High Energy Physics, Beijing 100049, China*
[3]*University of Chinese Academy of Sciences, Beijing 100049, China*
[4]*Sino-French Institute of Nuclear Engineering and Technology, Sun Yat-sen University, Zhuhai 519082, China*

Plastic scintillator (PS) embedding wavelength shifting (WLS) fiber is widely used in high energy particle physics, as muon taggers, and also in medical physics and other applications. In this work, a simulation package is built to evaluate the effects of the diameter and the layout of the optical fiber on the light yield with different configurations. The optimal optical configuration was designed based on the simulation and then validated with two PS prototypes under certain experimental conditions. In the study, the top veto tracker (TVT) of the JUNO-TAO experiment, comprised of 4 layers of 160 strips of PS was designed and evaluated. When a muon tagging efficiency of a PS strip is higher than 99%, the threshold is evaluated. The efficiency of 3-layer out of 4-layer of TVT will be higher than 99% even with the tagging efficiency of a single strip as low as 97% using a threshold of 10 p.e. assuming 40% SiPM PDE.

Keywords: Plastic scintillator, WLS-fiber, Light yield, Optical transmission performance, Muon tagging efficiency, JUNO-TAO.

I. INTRODUCTION

The collisions between the primary cosmic rays and the earth's atmosphere will produce a large number of muons[1], the average kinetic energy of which at the sea level is several GeV[2]. Because of the high energy, large mass, small deceleration and deflection in the electromagnetic field, and small bremsstrahlung effect with the atomic nuclear electric field in the matter, the muons will have a strong penetration power[3]. A sub-system of the muon veto detector with high muon tagging efficiency is very important to greatly reduce the background induced by the cosmic-ray (CR) muons for the experiments with only limited overburden near the ground, where the flux of muon is normally four to seven orders of magnitude higher than the underground laboratories with large overburden, such as Jinping underground laboratory[4], Gran Sasso underground laboratory[5] and Canfranc underground laboratory[6]. For example, in neutrino experiments[7–9], dark matter experiments[10–13], neutrino-less double beta decay experiments[14–16], those muon veto systems require muon tagging efficiency higher than 99%. At present, the detectors based on plastic scintillators (PS) have the advantage of easy machining[17–21], flexible structure design, efficient and stable performance[22, 23]. The PS detectors[24], especially with WLS fibers[25–30] and optical photodetectors (Multi-anode PMTs or Silicon PhotoMultipliers(SiPMs)), were used in OPERA[31], MINOS[32], LHAASO[33, 34] and many other experiments[35–38]. Meanwhile, the PS detectors have many applications in geological imaging[39–42], reactor monitoring and other fields[43–45].

The Taishan Antineutrino Observatory (TAO or JUNO-TAO) is a satellite experiment of the Jiangmen Underground Neutrino Observatory (JUNO)[8, 9]. The main purpose of the TAO experiment is to provide a precise neutrino energy reference spectrum for JUNO and benchmark measurements for the nuclear database. TAO detector system will consist of a central detector (CD), an outer shielding and a veto system. The CD will be placed at around 30 m from one core of the Taishan Nuclear Power Plant. The CD consists of a 2.8-ton gadolinium-doped liquid scintillator (LS) filled in a spherical acrylic vessel. The gadolinium-doped LS, as a target material, reacts with neutrinos from the reactor to measure the neutrino energy spectrum[46]. Because TAO only has a limited vertical overburden of 4 m of concrete, the major backgrounds for the TAO experiment are muon spallation products and accidental coincidences, mostly due to the natural radioactivity, the top veto tracker (TVT) requires to tag muons with an efficiency of higher than 99%.

In this paper, a comparison is realized in sec.II between a simulation based on Geant4[47–49] and a measurement of a prototype of a PS strip with WLS-fiber readout. The light yield results of the experiment and simulation are consistent for passing through muons. In sec.III, the diameter and the layout of the WLS fiber were further checked for higher light yield against with the simulation. An optimized design of the PS strip with WLS-fiber and SiPM readout is proposed for the TVT system of JUNO-TAO with high light yield and muon tagging efficiency, which will provide a good reference and guidance for the design of PS detector with WLS-fiber. At the same time, the reliability of the optimal design is preliminarily proved by experiments. In sec.IV, with the proposed PS strip design, the expected performance of the TAO TVT system is demonstrated. Finally, a summary is given in sec.V.

II. PROTOTYPE OF PS STRIP WITH WLS-FIBER AND SIMULATION

Muons will deposit their energy when they pass through and interact with the surrounding materials, and the process of muon energy loss is called muon ionization energy loss[3]. The average energy loss per distance (mass thickness) can be described by the Bethe-Bloth formula (1) [3, 50]:

$$-\frac{dE}{dx} = Kz^2\frac{Z}{A}\frac{1}{\beta^2}[\frac{1}{2}ln(\frac{2m_ec^2\beta^2\gamma^2W_{max}}{I^2}) - \beta^2 - \frac{\delta}{2}], \quad (1)$$

where K is a constant, z is the unit charge of the incident muon, m_e and c are the electron mass and the speed of light, respectively. Z and A are the atomic number and mass number of the passing-through matter. W_{Max} is the maximum kinetic energy that can be transferred to an electron when the muon collides with the atom. I is the average excitation energy of the matter. β is the ratio of the speed of a particle to the speed of light. γ is the lorentz factor. δ is the correction factor of the density effect of the matter. The above parameters are constant for a given matter.

From the formula (1), the deposited energy of muon in the material is related to the energy of muon and the atomic number of the material. For thin-layer media with an atomic number less than 20, such as a PS strip, muons almost pass through in a straight line. Partially lost energy of muon will be converted into light in a PS strip, and the light will be exported by the WLS-fiber, where SiPMs coupled with the fiber is an effective, convenient, and rapid method to pick up the photons and then convert them into an electrical signal.
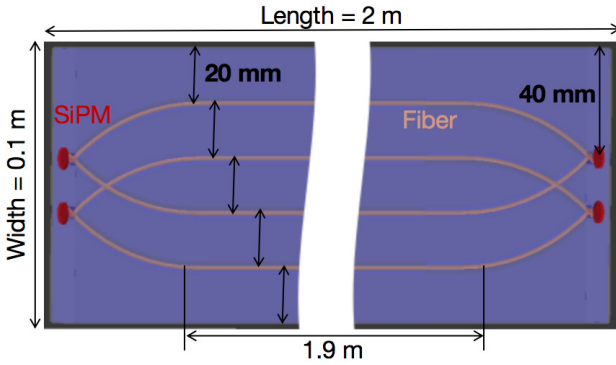

Fig. 1. Design of a prototype of the PS strip with WLS-fiber (Subsequently, it is named option 1)

A prototype of the PS with WLS-fiber readout is designed and fabricated as shown in Figure 1[51], named option 1. Its size is in a dimension of 2 m (Length)×0.1 m (Width)×0.02 m (Thickness), and four optical fibers with a diameter of 1 mm are used in total. The pink lines represent the WLS fiber equally spaced, inserted, and filled in the surface of the PS strip. The length of the straight portion is 1.9 m. The arrangement is symmetrical in both length and width directions. Two of the fibers are focused into a single group which can be coupled with optical sensors. This option can reduce the number of optical sensors. For example, four SiPMs (red circular point in the figure) can be used for each fiber group, or two PMTs can be used for each PS end. Finally, the PS is wrapped in reflective film (aluminum foil) except for the pips of the optical fiber to export photons, and more details can be found in Ref[51]. The current prototype was tested with CR muon before design optimization.

A CR muon survey along the length of the PS strip prototype with PMT/SiPM is done with the schema shown in Figure 2 (the arrangement of optical fibers is not shown). The CR muon[28, 52] will be selected by the two muon monitors of small scintillators on different hitting locations. When the CR muon monitors are triggered, the signals of the PS strip will be recorded too. 9 points equally spaced along the strip were measured in total relative to the center of the PS. More details about the experiment can be found in Ref [51]. The PS strip is fabricated by Beijing Hoton Nuclear Technology Co. Ltd [53]. The type of fiber is the WLS fiber BCF92 [54, 55]. For further understanding and optimization, a Monte-Carlo (MC) simulation project is set up based on Geant4[47, 49, 52] with the parameters provided by the manufacturer of the PS, the reflective film and WLS-fiber [55, 56]. The simulation project mainly includes three parts: the first part is the detector geometry, and the PS geometry with optical fibers is designed through a geometric interface. This is why there are various geometric designs in subsequent optimizations. The second is the physical process section, which contains a physical list and the optical processes of optical photons. The physical list includes such things as ionization, bremsstrahlung, multiple scattering, pair generation, Compton scattering, and photoelectric effects. Optical processes include the generation of Scintillation and Cherenkov light, wavelength shift effects, Rayleigh scattering, bulk absorption, and boundary processes. The third is the extraction and analysis of information. The PS and PMT/SiPM are set as sensitive areas; The PS is responsible for obtaining information about the muon, and the PMT/SiPM is responsible for obtaining information about the photons hitting. A parameter interface is provided in the simulation package to set the properties of the material, such as the PS attenuation length, the scintillator yield (refers to the number of photons generated when the energy deposited in the scintillator is 1 MeV), the reflectivity of reflective film. By scanning these parameters, a series of simulation responses, including the light yield (referring to photoelectron (p.e.) with consideration of the corresponding photon detection efficiency (PDE)/quantum efficiency (QE) of SiPM/PMT) along the PS longitudinal direction, is obtained. χ^2 analysis is performed with the experimental data. Table 1 presents a list of parameters corresponding to the minimum χ^2. In the subsequent optimization work, the parameters of PS, optical fiber and reflective film in table 1 are the same in simulation.

The comparison of light yield between the measurement and simulation at different positions is shown in Figure 3(a), where the light yield (in p.e.) refers to the average value of the photoelectron distribution of the selected muons hitting each position and the X-axis represents the distance from the
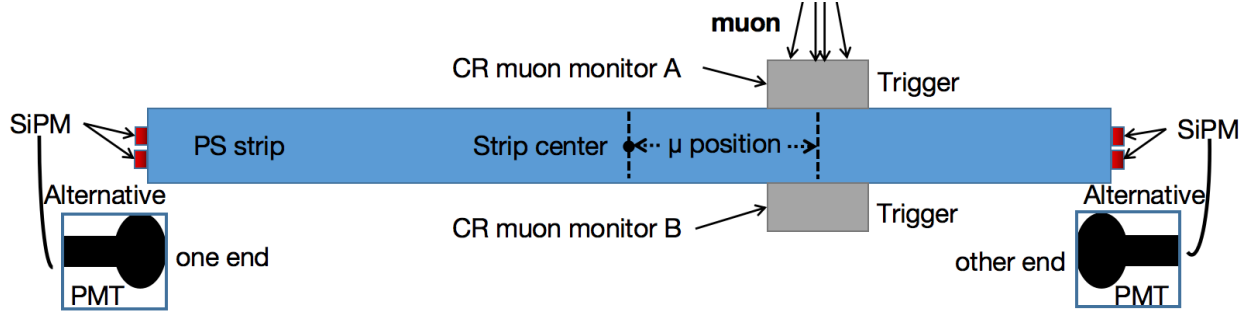
Fig. 2. Device and principle diagram for CR muon measurement with the PS strip prototype. The CR muon will be selected by the two muon monitors of small scintillators on different hitting locations. When the CR muon monitors are triggered, the signals of the PS strip will be recorded too.
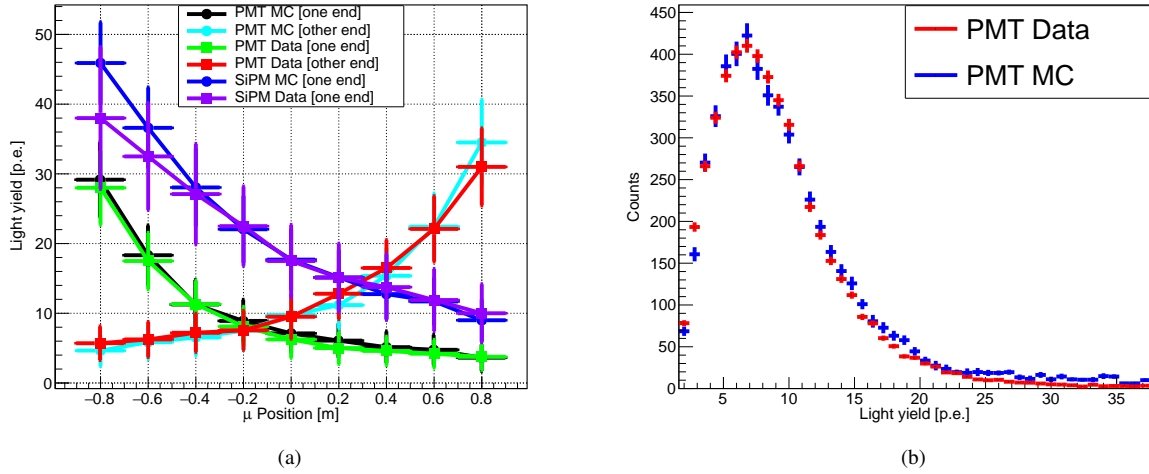

(a)

(b)

Fig. 3. (a): Comparison of light yield between measurement and simulation at different muon hitting positions. The horizontal error bar is from the dimension of the muon monitors, and the vertical error bar in MC is the statistical error. Due to the different QE of PMTs and coupling, light yield at the two ends is not strictly symmetrical. The light yield of SiPM is larger than that of PMT. Based on the advantages of compact requirements, robustness, and higher light yield than PMT, SiPM is proposed as a sensor for TVT. (b): When the CR muon monitor in the center of PS, a comparison diagram of the experimental energy spectrum and simulation of PMT at one end.

Table 1. The key parameters of the simulation of the PS strip prototype

Material	Properties	Parameters
PS	Base	Polyvinyltoluene
	Scintillation yield (photons/MeV)	8000
	Emission peak (nm)	415
	Attenuation length (cm)	200 @ 400 nm
WLS-Fiber	Core	Polystyrene
	Attenuation length (cm)	380 @ 400 nm
Reflective film	Base	Aluminium
	Reflectivity	85%

158 center of the PS strip in the length direction. When using the
159 PMT as the sensor, the simulation and data are in good agree-
160 ment within the error. The light yield at both ends should be
161 symmetrically distributed around the center of the PS. Due

162 to the different QE of PMT, the light yield at the two ends is
163 not strictly symmetrical. When using SiPM of the same type
164 as a sensor, the distribution of the light yield at one end is
165 shown here. As can be seen from the figure, the light yield
166 of SiPM is larger than that of PMT. Based on the advantages
167 of compact requirements, robustness, and higher light yield
168 than PMT, SiPM is proposed as a sensor for TVT. In addition
169 to the initial comparison shown in Figure 3(a), another simi-
170 lar comparison of energy spectra is also obtained between the
171 measurement and simulation at center of PS shown in Fig-
172 ure 3(b), except for individual energy points that do not con-
173 form to the experiment, others are in good agreement with
174 the experiment within the error range. From an experimental
175 perspective, each PMT/SiPM has a different QE/PDE, Since
176 the following optimization work does not pay attention to the
177 impact of electronics, in subsequent studies, the QE of each
178 PMT or the PDE of SiPM will be input with the same value.

III. OPTIMIZATION OF PS STRIP LAYOUT

On the basis of the agreement between experiment and simulation, a further study on the configurations of the PS strip design is done including the diameter and the arrangement of the WLS-fiber for the light yield and tagging efficiency. The relationship between the light yield and fiber diameter is shown in Figure 4 for 2 PS configurations with the same number of fibers embedded. Each point refers to the light yield of the muon hitting the PS center. The magenta heart represents the measurement of the prototype with PMT mentioned earlier. The simulated relationship between the light yield and the fiber diameter was represented by red lines with a PS width of 100 mm and a spacing of approximately 20 mm between neighbor fibers. On the other hand, the blue lines represented the simulated relationship with a PS width of 200 mm and a spacing of around 40 mm between neighbour fibers. Most photons are collected through the WLS fiber by the sensors. Since the area of the optical sensor (Since TAO TVT requirement for readout, subsequent optical sensors default to SiPMs) is larger than the dimension of the optical fiber, there are still some PS scintillation photons directly collected by the sensors without going through the WLS fiber. The two straight lines at the bottom represent the photons directly from the PS scintillation to the SiPM, where the light yield contributed by the PS itself is basically independent of the fiber diameter.

According to the trend of the plot, the larger the fiber diameter, or the smaller spacing of the neighbor fibers, the higher the light yield. Finally, a 1.5 mm fiber diameter is suggested according to the expected response and reasonable cost.

Following the requirements of the JUNO-TAO TVT system, the PS strip with 20 cm width is suggested according to the fabrication, electronics, and cost, but there is still more than one option proposed following a different strategy as shown in Figure 5. The length and thickness of all the options are the same as 2 m, and 20 mm is a basic requirement. The width of option 2, option 3, option 3-1, and option 4 are 200 mm, while the width of option 1 is only 100 mm as the measured prototype. The number of fibers is eight to have a similar spacing except option 1. The fiber of option 2 is only arranged on the front of the PS as doubled of option 1. Option 3 is similar to option 2, but with four optical fibers installed on the back and another four on the front of the PS, respectively. The fiber layout of option 3-1 and option 4 are in a different arrangement. The fiber of options 3-1 is more uniform than that of option 2, but it is not staggered like that of option 4. For option 1, option 2, and option 3, the length of the straight portion of the fiber is 1.9 m. For option 3-1 and option 4, the length of the straight portion of the fiber is 1.5 m.

The PS width and WLS fiber diameter of all the options are listed in table 2. The performance (mainly on the light yield and muon tagging efficiency) and differences among the proposals were further evaluated by simulation. It can be divided into three categories for comparative study.

For Option 2 VS. Option 3: addresses the dependence of light yield on fber placement.

For Option 2 VS. Option 3-1: addresses the basic dependence of light yield on the uniformity of the fber arrangement in the PS.

For Option 2 VS. Option 4: addresses the dependence of light yield on the fber layout.

A. Light yield: nPhotons × PDE

The angular distribution of the CR muon hitting the PS will affect the PS response. To check the difference and eliminate the additional influence of angular dependence, the muons that are vertically and uniformly incident on the PS strip are used in the simulation firstly. The results of the number of photons received by SiPM for option 1-4 are shown in Figure 6(a). The X-axis is the number of photons (nPhotons, light yield = nPhotons × PDE): the sum of the photons collected by all the SiPMs in a muon event. The figure also shows the average number of photons received by all SiPMs for all muon events. The black line is the distribution of the photons collected by SiPM of option 1. The red and the green lines represent the photon number distributions of option 2 and option 3, which overlap, indicating that the back or front location of fibers has no obvious effect on the collection of the photons. The recieved photons of the fiber is from the absorption and reemission, reflection of the Cerenkov photons of PS rather than the directly generated photons. The average value of nPhotons in option 2 is almost twice that of option 1. Option 4 has more nPhotons than the previous three options, which indicates that the arrangement of fibers has a large impact on the light yield. The difference of nPhotons between option 4 and option 2 is studied in detail in section III B. All the plots have the same entries, therefore the maximum height of the plots is related to the distribution width.

Another simulation is done to evaluate the differences between option 2, option 3-1, and option 4. The muon generator here is updated in energy and angular distribution according to the Ref.[57, 58] as a more realistic situation to model the response of the PS strip. The results are shown in Figure 6(b). The black, blue, and red lines represent the total photon number distribution of option 2, option 3-1, and option 4, respectively. The figure also shows the average value of photons received by all SiPM of all muon events. Except for the total number of photons, the average value of photons of option 4 is the highest, option 3-1 is the middle, and option 2 is the lowest. Option 4 has the best ability to collect photons.

From the formula (1), it can be known that the deposited energy is directly proportional to the track length of muon

Table 2. Main configurations of different options of PS strip layout

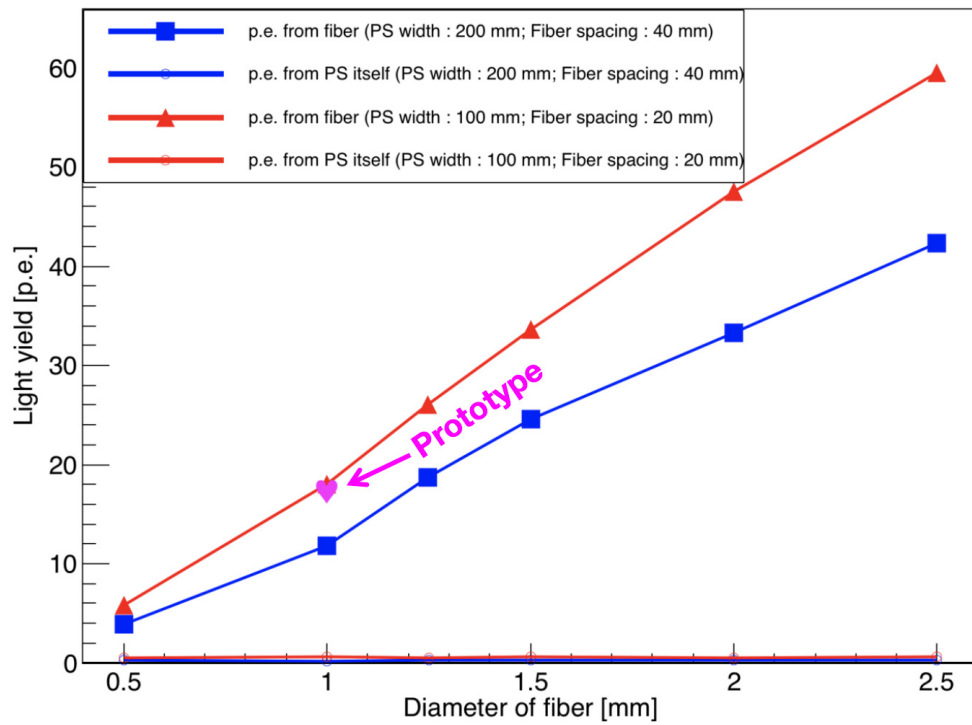| Configuration	option 1	option 2	option 3	option 3-1	option 4
PS width (mm)	100	200	200	200	200
Fiber numbers	4	8	8	8	8
Fiber diameter (mm)	1	1.5	1.5	1.5	1.5
Fiber spacing (mm)	20	20	20	24	22.5

chinaXiv:202302.00256v2

Fig. 4. Assuming 30% SiPM/PMT PDE/QE; each point refers to the light yield of the muon hitting the PS center. The magenta heart represents the measurement of the prototype with PMT mentioned earlier. Two widths of 200 mm and 100 mm for the PS are checked with the same length of 2 m and thickness of 0.02 m. The simulated relationship between the light yield and the fiber diameter was represented by red lines with a spacing of approximately 20 mm between neighbor fibers. The blue lines represented the simulated relationship with a spacing of around 40 mm between neighbour fibers. The same four fibers are used in each case, which is why the light yield of the 200 mm wide PS is smaller than that of the 100 mm one.
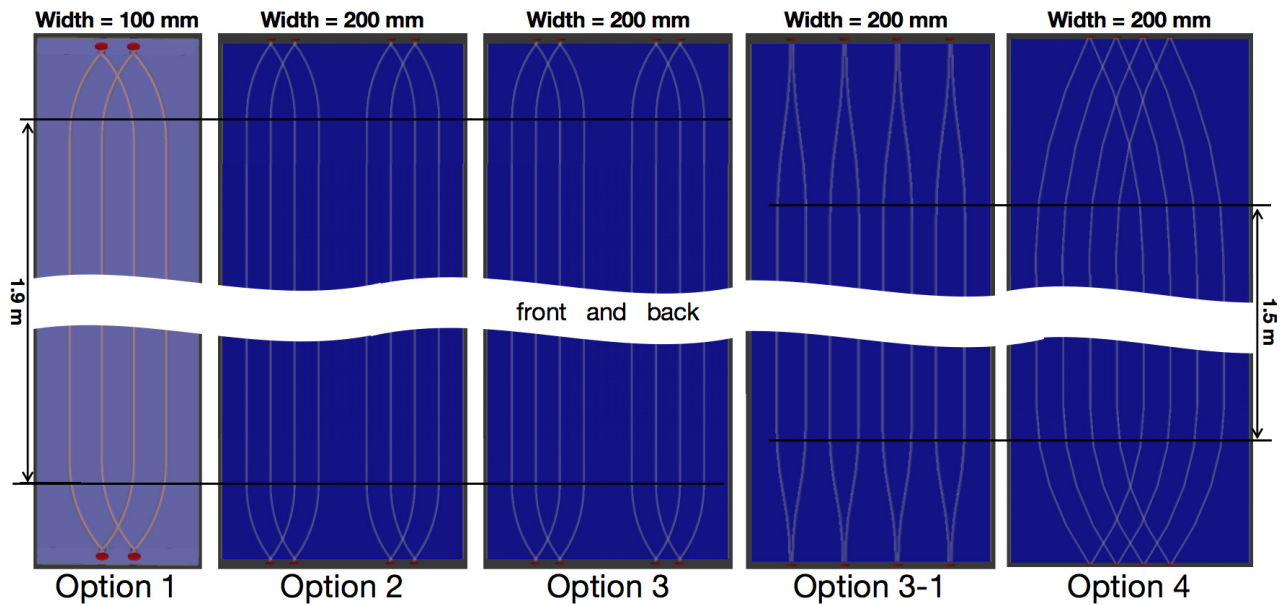

Fig. 5. All evaluated designs of a single PS strip. The number of fibers is eight with a similar spacing except option 1. The fiber of option 2 is only arranged on the front of the PS as doubled of option 1. Option 3 is similar to option 2, but with four optical fibers installed on the back and another four on the front of the PS, respectively. The fiber layout of option 3-1 and option 4 are in a different arrangement. The fiber of options 3-1 is more uniform than that of option 2, but it is not staggered like that of option 4.
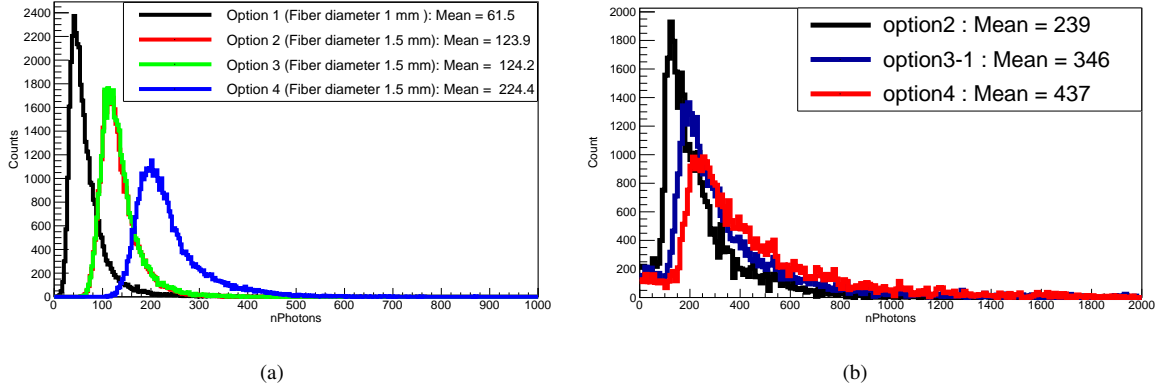
(a)

(b)

Fig. 6. (a): With vertical incident muon simulation: Distribution of total number of photons received by SiPM for four different options of PS strip layout.nPhotons: the number of photons received/collected by all the SiPMs in a muon event, without the consideration of the corresponding PDE of SiPM. Light yield = nPhotons × PDE; the average value of nPhotons in option 2 is almost twice that of option 1. Option 4 has more nPhotons than the previous three options.(b): With realistic muon simulation: Distribution of the total number of photons received by SiPM with different fiber arrangements. The black, blue, and red lines represent the total photon number distribution of option 2, option 3-1, and option 4.
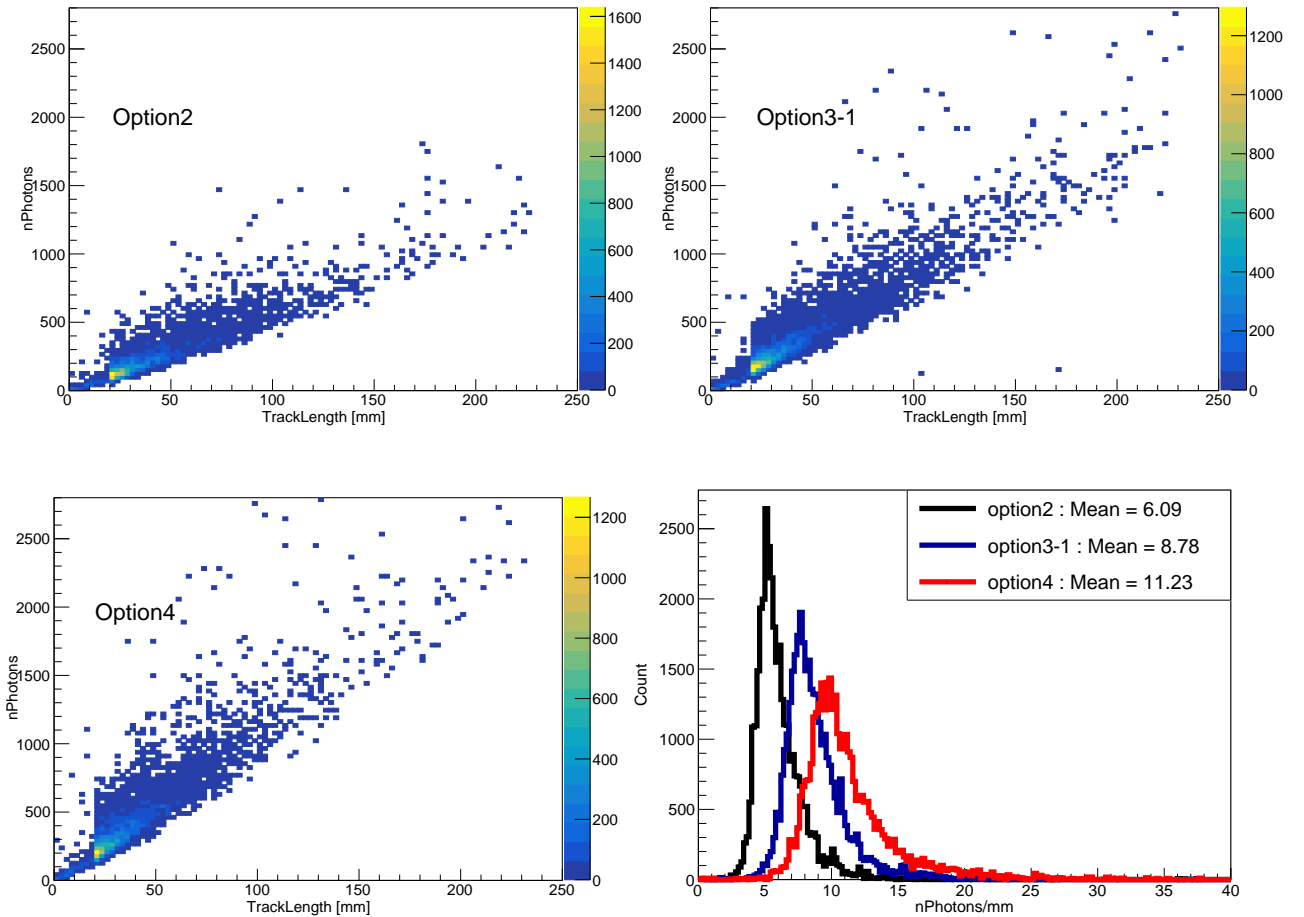

Fig. 7. Total photon number versus muon track length. The upper left, upper right, and bottom right of the picture represent the two-dimensional diagram of total photon number versus muon track length for option 2, option 3-1, and option 4 respectively. Bottom right: comparison of the photon number normalized to unit muon track length.

passing through the material. Because of the oblique incidence of muons of the updated muon generator in the second simulation, the track length of the muons in the PS strip can be either less(represent an edge events) or greater than the thickness of the PS strip. The total photon number in Figure 6(b) is much higher than that in Figure 6(a) even with the same option: the average value of nPhotons has nearly doubled, while some signals with small amplitude show up. The upper left panel of Figure 7 shows the two-dimensional diagram of total photon number versus muon track length for option 2, the upper right panel is for option 3-1, and the bottom left panel is for option 4. The colors of the three panels represent the density of events. The total photon number is proportional to the track length as expected. When the track length is 20 mm (thickness of the PS), the event density is the highest due to the maximum flux density when muon is vertically incident. The bottom right panel of Figure 7 shows the photon number per millimeter of muons passing through the PS strip of the three options. It is obvious that the average value of photons per unit length (mm) of option 4 is 11.23, which is nearly twice that of option 2. This concludes that option 4 is the most effective one for the light yield response to muon when the muon deposits the same amount of energy among these options.
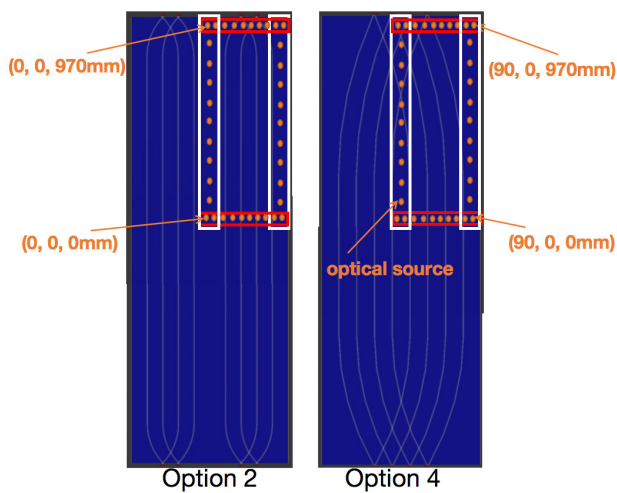
B. Transmission performance

Fig. 8. Position distribution diagram of optical scanning of option 2 and option 4: the two white frames indicate the simulated points of 11 different positions along the length direction of the PS, respectively; and the two red frames indicate the simulated points of 10 different positions along the width direction of the PS, respectively. Each point is equidistant.

Option 2 and option 4 have a similar configuration on WLS-fiber number, PS length, width, and thickness, but their light yields show an obvious difference. The photon transmission process is further checked for a better understanding of any specific reasons for the influence of fiber arrangement on the light yield for possible further optimization.

Muon deposits its energy along its track in the PS and emits photons in four π directions. Meanwhile, the photons in the PS will propagate through attenuation, absorption, and re-emission effects, so it is not easy to accurately characterize the light transmission performance between different options. A specified optical survey is done to check the photon refection times before absorption by the WLS-fiber of each photon generated by PS, where the survey locations are shown in Figure 8 trying to cover the center and edge of the PS strip. The orange points are the specified locations to generate optical photons. At each point, 15000 photons are generated in four π directions to mimic the random photons excited by a muon. It is obvious that before the photons enter the fiber, more reflection times, more difficult to reach SiPM (inverse relationship). At the same time, if the number of photons entering the fiber is more, the number of photons arriving at SiPM is more (proportional relationship). In order to model the combination of the two factors, an R-value proposed as the total number of photons entering the fiber divided by the average number of reflections of photons before entering the fiber.

Figure 9 shows the distribution of R-value of an optical survey at different positions under option 2 and option 4. The abscissa of each point is the position corresponding to the dash # symbol in the figure, the specific location can be seen in combination with Figure 8. The ordinate of each point is the R-value stands for optical transmission performance. The red line is the R-value of option 4, and the black represent option 2. The upper left panel of the figure shows the distribution of the R-value along the length direction of the PS strip when the position is the center of the width of the PS. The R-value of option 4 is higher than option 2 in the whole length direction. The lower left panel shows the distribution of the R-value along the length direction of the PS strip when the position in the edge of the width of the PS strip. The R-values of the two are nearly the same, except for the edge in the length direction, where the R-value of option 2 is greater than option 4. The upper right panel reveals the distribution of the R-value along the width direction of the PS when the position is the center of the length of the PS, where option 4 and option 2 have a trend of trade-offs. The lower right panel reveals the distribution of the R-value along the width direction of the PS when the position is the edge of the length direction of the PS, the R-value of option 4 is larger than that of option 2 at the positions within 30 mm from the middle in the width direction of the PS.

The results show that when the photon is generated at a location where the fiber is sparse, the number of photons entering the optical fiber will decrease sharply, while the times of reflections will also increase. Meanwhile, when photons is generated in dense places of fibers, the number of photons entering the fiber will increase dramatically, while the times of reflections will also decrease dramatically.

Looking at the four figures as a global picture, with option 2 configuration, the maximum vertical coordinate of the black point is less than 200, but with option 4 configuration, the ordinate of the red point can be greater than 200. The R-value of option 4 and option 2 has a trend of trade-offs and
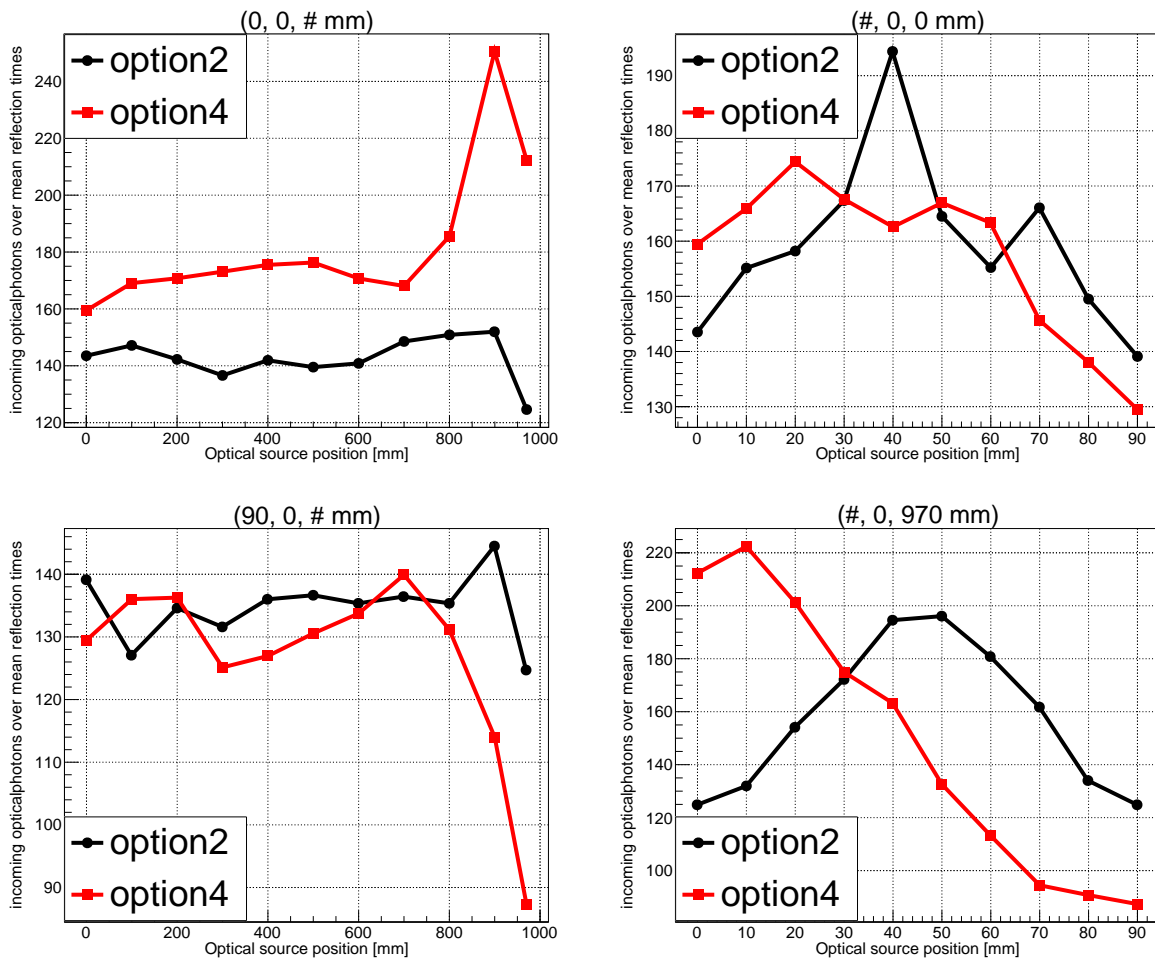
Fig. 9. The distribution of the ratio of the photon numbers entering the fiber to the average times of reflections at different positions of the optical survey. The value of the X-axis of each point is the position corresponding to the dash # symbol in the graph, and the value of the Y-axis of each point in the graph represents the R-value. The upper left panel of the figure shows the distribution of the R-value along the length direction of the PS strip when the position is the center of the width of the PS. The R-value of option 4 is higher than option 2 in the whole length direction. The lower left panel shows the distribution of the R-value along the length direction of the PS strip when the position in the edge of the width of the PS strip. The R-values of the two are nearly the same, except for the edge in the length direction, where the R-value of option 2 is greater than option 4. The upper right panel reveals the distribution of the R-value along the width direction of the PS when the position is the center of the length of the PS, where option 4 and option 2 have a trend of trade-offs. The lower right panel reveals the distribution of the R-value along the width direction of the PS when the position is the edge of the length direction of the PS. The results show that when the photon is generated at a location where the fiber is sparse, the number of photons entering the optical fiber will decrease sharply, while the times of reflections will also increase. Meanwhile, when photons is generated in dense places of fibers, the number of photons entering the fiber will increase dramatically, while the times of reflections will also decrease dramatically.

the overall difference is small from the lower left and upper right panel of Figure 9. The R-value of option 4 and option 2 has a big difference from the upper left and lower right panel of Figure 9. The distribution of R values in the PS region has been get. To obtain a quantitative relationship between the optical transmission performance of option 2 and option 4 in the entire region, an explanation of mathematical integration (R-value) were provided. The integral area under the red and black lines in the upper left and lower right panels of Figure 9 is calculated. Then, the integral area of the red line in the upper left panel is multiplied by the area in the lower right panel to obtain the transmission performance of the whole region of option 4. The same procedure is followed for the black line as for the red line, and the product of the two integral areas is used as the transmission performance of the entire region of option 2. Finally, the product of the integral area of the red line is divided by the product of the black line, and it is found that the ratio is 2.21. This shows that the transmission performance of the whole area of option 4 is 2.21 times better than that of option 2. Therefore, it can be understood why the overall photon number of option 4 is more than that of option 2. At the same time, the curve shows that the R-value distri-

bution range of option 4 is larger than that of option 2, which means that the optical export uniformity of option 4 is worse than that of option 2. This is the result of uneven optical fiber layout.

In short, it was found that if the optical fiber in the PS middle region is in higher density, the final effective light yield will be higher. Therefore, to achieve a higher light yield, it is possible to consider placing as many optical fibers as possible in the middle of the PS.

So far, in terms of light yield, many simulations and made massive comparisons have done, the best configuration has been obtained that is option 4 under the current design conditions. At the same time, to some extent, the reason why it is the best option has been quantitatively explained and good reference and guidance suggestions for the processing technology and structure design were provided. For a PS detector, the most important factor, in addition to light yield, is the muon tagging efficiency. In the next section, the muon tagging efficiency and inefficiency are discussed.

C. Muon tagging efficiency and inefficiency

To simplify the simulation process, assuming that the PDE of SiPM is equal to 30%. The sum of four SiPM outputs at both ends can be acquired under different options to further study the muon tagging efficiency. Figure 10 shows the two-dimensional distribution of light yield at both ends of option 2, option 3-1, and option 4 in simulation, respectively. The abscissa is the sum of the SiPM outputs at one PS end, and the ordinate is the sum at the other end. The range of light yield at both ends of option 4 is the strongest and most divergent. If the sums at both ends of an event are greater than their respective threshold at the same time, it is considered that this muon has been detected. The event count of muon hitting the PS strip is noted as N_{all}, with the event count of detected muon noted as N_{tag}. The muon tagging efficiency is defined by the ratio N_{tag}/N_{all}. Here, the environmental background is not considered, mainly to eliminate environmental background interference. Figure 11 shows the relationship between the muon tagging efficiency and the threshold of option 2, option 3-1, and option 4, respectively. The black, blue and red represent the relationship between efficiency and threshold when the PDE of SiPM is 20%, 30% and 40%, respectively. As seen from the three figures, when PDE is 20% and the threshold is set to 10 p.e., the tagging efficiency of option 4 is still higher than 90%, while option 2 and option 3-1 are both less than 90%. With the increase of the threshold, the efficiency of option 2 decreases fastest, followed by option 3-1, and option 4 is the slowest. According to Figure 11, the required threshold can be found when a certain tagging efficiency needs to be achieved.

Figure 12 shows the corresponding threshold when the muon tagging efficiency reaches 99% under different PDEs of SiPM. When the PDE of SiPM is 40%, for option 2, the threshold cannot exceed 1.5 p.e.; for option 3, it cannot exceed 2.4 p.e.; however, for option 4, the threshold can be set to 3 p.e., which greatly reduces the contribution from dark noise of SiPM. So far, option 4 is superior to other options in terms of light yield and muon tagging efficiency. Therefore, Option 4 is taken as the current optimal configuration. When the PDE of SiPM is 40%, The threshold and corresponding tagging efficiency of a single PS strip were summarized in table 3.

Table 3. Threshold and corresponding tagging efficiency of single PS strip with 40% SiPM PDE.

Threshold(p.e.)	3.1	6.3	10	15	19
Tagging efficiency	99%	98%	97%	96%	95%

To further verify the simulation, another prototype with option 4 was built, the parameters of PS, optical fiber and reflective film are the same with before prototype in simulation. Only the PDE of the backend SiPMs is different. 2 SiPM were used as sensors and using the oscilloscope to collect data. The SiPM is from the K-series MicroK-40035-TSV[59]. The data is saved by the lecroy-HDO4104A oscilloscope. Preliminary experimental results were obtained.

Figure 13 shows the experimental measurement and simulation results of the PS prototype of option 4 when the muon monitor is in the PS center. To avoid the effect of the SiPM dark noise and environment background. Signals stronger than 3 p.e. was analyzed, and the blue line is the energy spectrum of one SiPM from the measurement. The red line is the result of the simulation. Every point has an error bar, the abscissa is the light yield, and the ordinate is the log stand for the normalized event rate. It can be seen from the figure that in the spectrum below 12 p.e., the simulated spectrum almost corresponds to the experiment. It was found that the most probable signal amplitude for passing through muons is around 8 p.e. from data. So for the final configuration used for TAO where there are 4 SiPMs at each end of the PS strip, the sum of the most probable signal amplitude will be about 32 p.e. When the spectrum is in the range of 15 p.e. to 25 p.e., within the range of error, the event rate of the simulated spectrum is more than that of the experiment. When the spectrum is greater than 25 p.e., and the event rate of simulation and experiment events is relatively small. In the high energy region, the energy spectrum does not show good consistency, but it does not affect our optimization work. Several main factors lead to differences in the energy spectrum. The first is that the coupling between SiPM and PS is not perfect and the same for simulation and measurement. The second is that the widths of the two small plastic modules for CR monitors are not the same, which may lead to a deviation of several centimeters in the location where muon hits. Resulting in an impact on the energy spectrum.

In any case, the light yield of option 4 is indeed much higher than that of option 1 before optimization. This shows that our optimization method is effective. According to the above analysis and design, The light yield and the muon tagging efficiency corresponding to option 2, option 3-1, and option 4 have been obtained. When the muon tagging efficiency reaches 99%, option 4 has the highest threshold limit.

To study and discuss the inefficiencies by simulation, the track length of all muons in the PS has been counted. The
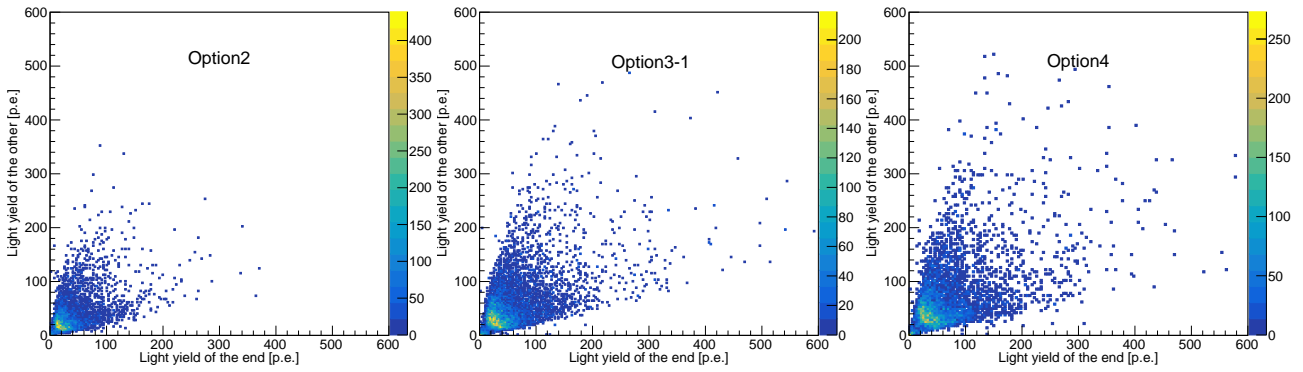
Fig. 10. Assuming 30% SiPM PDE. From left to right: two-dimensional distribution of light yield at both ends of option 2, option 3-1 and option 4, respectively. The color represents the density of events. From options 2 to 4, the distribution range of light yield gradually widens.
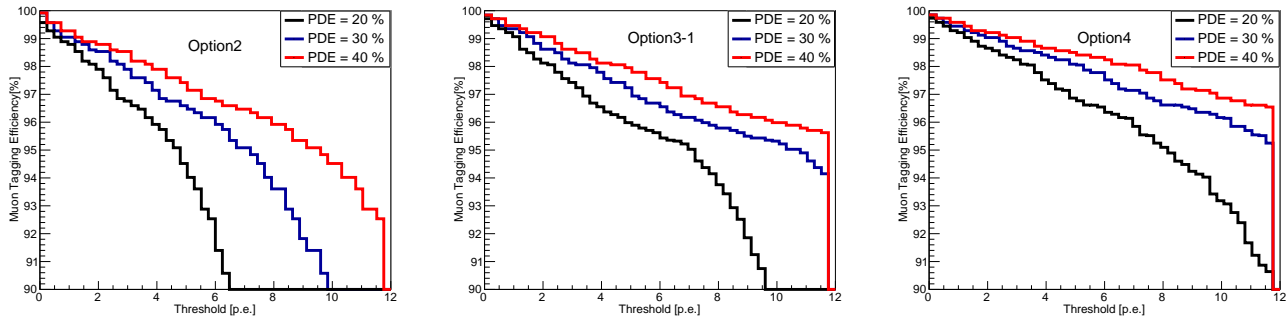

Fig. 11. Relationship between the muon tagging efficiency and the threshold of option 2, option 3-1, option 4, respectively. Where the threshold represents the sum of the SiPM of each PS end over threshold individually. As the threshold increases, the muon tagging efficiency of option 4 decreases the slowest.

Fig. 12. When the muon tagging efficiency requirement is 99%, the corresponding threshold limits for options 2, 3-1, and 4 respectively. When the PDE of SiPM is 40%, for option 4, the threshold can be set to 3 p.e., which greatly reduces the contribution from dark noise of SiPM.

inefficiencies can be indirectly explained by distribution of track length.

Figure 14 shows the ratio of the muon events whose track length exceeds certain threshold out of the total events under option 2, option 3-1, and option 4. The trends are almost the same and the difference in ratio was within 1%. The muon generator, the thickness, length, and width of the PS strip are the same for the three configurations, and the declining trend of the event ratio is basically consistent under the three configurations. The black horizontal dotted line shows the proportion of 99%, from which it can be obtained that the track length threshold of the corresponding black vertical dotted line is 3 mm. There are 1% muon events whose track length in the PS strip is less than 3 mm. Since the thickness of the PS is 20 mm, it is certain that the 1% muon events are incident at a large zenith angle and pass through the edge of the PS, which is often referred to as the edge event. Then, if building a module of PS to stagger the PS up, down, left and right, these edge events should also leave longer tracks on the next layer or the PS next to them, so as to be triggered. Thus, for a PS strip, the edge event may not be tagged(detected), but for the whole veto module system, it can be tagged. Therefore, under the same threshold, the muon tagging efficiency of a single layer module is higher than that of a single PS strip.
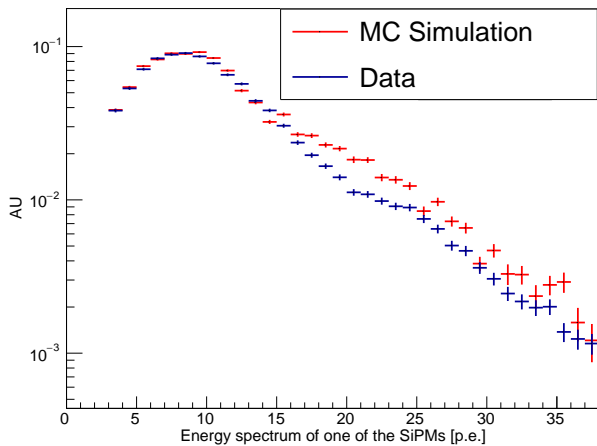
Fig. 13. Comparison between the simulation and experiment in terms of the energy spectrum for option 4. Assuming 40% SiPM PDE in MC. The PDE of the SiPM sample provided by the manufacturer is 46% at the wavelength of 420 nm when the working voltage is 37.2 V. The data is recorded when the CR muon monitor is in the center of PS.
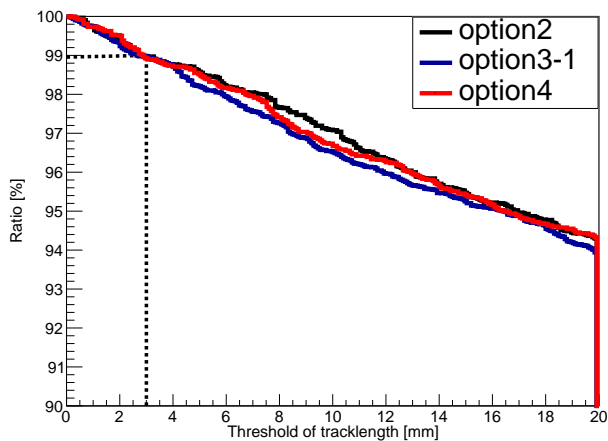

Fig. 14. Event ratio which the track length of incident muon in PS strip exceeds the threshold in the total events under option 2, option 3-1, and option 4, respectively.

₅₂₄ Based on this point of view, the JUNO-TAO top veto system
₅₂₅ was designed, called top veto tracker (TVT).

IV. PERFORMANCE OF JUNO-TAO TVT

₅₂₇ Figure 15(a) is the design schema of the TVT. The left
₅₂₈ panel of Figure 15(a) shows the side view of the whole 4-
₅₂₉ layer PS, the seam of the upper layer of PS corresponds to the
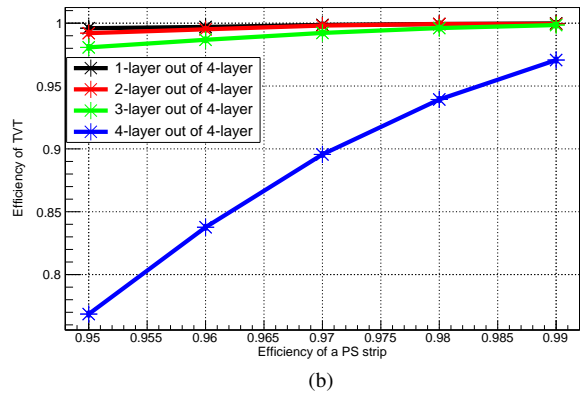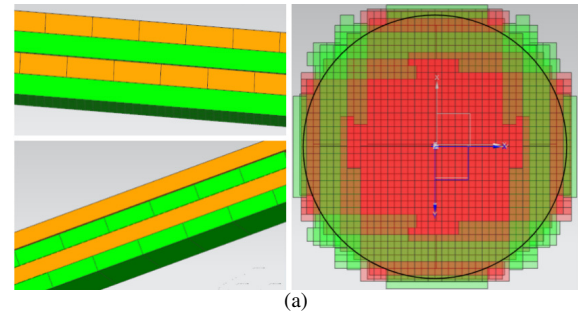₅₃₀ volume of the next layer of PS, which can eliminate the dead

Fig. 15. (a): Design of JUNO-TAO TVT. The left panel is a side view. The right panel is a top view.(b): Muon tagging efficiency of hitting multi-layer PS with that of single.

₅₃₁ space. At the same time, it is considered that the track direc-
₅₃₂ tion of a muon can be determined by this system. Therefore,
₅₃₃ a 4-layer PS is designed, and the gap between neighboring
₅₃₄ layers is 2 cm. (It refers to the gap between the SiPM end of
₅₃₅ one PS and the end of another PS). The right panel of Figure
₅₃₆ 15(a) shows the top view of the whole 4-layer PS. Different
₅₃₇ colors represent different layers of PS. Since the central de-
₅₃₈ tector of TAO is a ball, under the condition of saving funds
₅₃₉ and consumables. Our best effort is to cover the ball's projec-
₅₄₀ tion surface with the area of PS, resulting in the formation of
₅₄₁ a circle by the four layers.

₅₄₂ Figure 15(b) shows the distribution of the muon tagging ef-
₅₄₃ ficiency of hitting multi-layer PS versus that of a single PS.
₅₄₄ The different colors represent the efficiencies of hitting the
₅₄₅ different number of layers of PS. The black line represents
₅₄₆ the muon tagging efficiency of any one out of four layers.
₅₄₇ The red represents any two out of four layers. Because the
₅₄₈ gap between each layer is very small, the red and black lines
₅₄₉ almost coincide a PS strip efficiency. The blue represents the
₅₅₀ muon that hits the whole four layers and is also tagged by the
₅₅₁ four layers of PS. Since each layer has a certain dead space,
₅₅₂ as the efficiency of the PS strip decreases, the tagging effi-
₅₅₃ ciency reduction on all four layers will be most noticeable.
₅₅₄ The green represents any three out of four layers, from which
₅₅₅ this conclusion can be obtained: even if the efficiency of a PS
₅₅₆ strip is as low as 97%, which is equivalent to the threshold of
₅₅₇ 10 p.e. can be found in Table 3, the muon tagging efficiency

of any three out of four layers will still be higher than 99%. In addition, by simulating the environment background (including ^{238}U, ^{232}Th, ^{40}K chain), the background event rate that can pass the 3 p.e. threshold in any two out of four layers of PS is 1280 ± 40 Hz and the rate that can pass the 3 p.e. threshold in any three out of four layers of PS is < 10 Hz. Therefore, the condition can be selected wherein any three out of the four layers are triggered to tag muon and reject the background.

V. SUMMARY

There are numerous PS with WLS-fiber options with different configurations. In this paper, through simulation package, the differences between different configurations are checked in detail, for example, for the influence of optical fiber diameter, layout and other factors on transmission performance. Based on light yield and muon tagging efficiency, the optimal configuration of WLS-fiber PS under certain conditions is obtained. The relevant bench test of option 1 and option 4 has been measured, in terms of the most probable SiPM output, the summed signal at one end of the optimized option 4 is about 32 p.e.. The light yield is 4 times larger than option 1, which further verified the reliability of the simulation package.

At the same time, inefficiency muon events are also studied. Finally, the design scheme of JUNO-TAO TVT system is reached. These conclusions can be given in the simulation: Assuming 40% SiPM PDE, the muon tagging efficiency of a single PS strip at a 3 p.e. threshold can still reach 99% in "AND" mode(i.e., when signals above the threshold were required from two sides of a PS strip.), the background event rate that can pass the threshold in any three out of four layers of PS is less than 10 Hz(Almost zero). When the threshold is 10 p.e., the muon tagging efficiency of a single PS strip is 97%, The efficiency of 3-layer out of 4-layer of TVT will still be higher than 99%.

[1] P.A. Zyla, et al. (Particle Data Group). Review of Particle Physics. Progress of Theoretical and Experimental Physics. **08**, 08 (2020) DOI:10.1093/ptep/ptaa104

[2] Mengyun Guan and Ming-Chung Chu and Jun Cao and Kam-Biu Luk and Changgen Yang. A parametrization of the cosmic-ray muon flux at sea-level. DOI:10.48550/arXiv.1509.06176

[3] Patrignani, C. and others. Particle Data Group. Review of Particle Physics. Chin. Phys. C. **10**, 100001 (2016). DOI:10.1088/1674-1137/40/10/100001

[4] Zi-yi Guo and Lars Bathe-Peters and Shao-min Chen and (JNE Collaboration). Muon flux measurement at China Jinping Underground Laboratory. Chinese Physics C. **45**, 025001 (2021). doi:10.1088/1674-1137/abccae

[5] E. Barbuto and C. Bozza and M. Cozzi and et al. Atmospheric muon flux measurements at the external site of the Gran Sasso Lab. Nuclear Instruments and Methods in Physics Research Section A: Accelerators, Spectrometers, Detectors and Associated Equipment. **525**, 485-495 (2004). doi:https://doi.org/10.1016/j.nima.2004.01.078

[6] Trzaska, Wladyslaw Henryk and Slupecki, Maciej and Bandac, et al. Cosmic-ray muon flux at Canfranc Underground Laboratory. European Physical Journal C. **79**,8 (2019). doi:10.1140/epjc/s10052-019-7239-9

[7] JUNO Collaboration. JUNO physics and detector. Progress in Particle and Nuclear Physics. **123**, 0146-6410 (2022). doi:https://doi.org/10.1016/j.ppnp.2021.103927

[8] JUNO Collaboration and T. Adam et al. JUNO Conceptual Design Report. physics.ins-det. https://ui.adsabs.harvard.edu/abs/2015arXiv150807166A

[9] JUNO Collaboration and Angel Abusleme et al. TAO Conceptual Design Report: A Precision Measurement of the Reactor Antineutrino Spectrum with Sub-percent Energy Resolution. physics.ins-det. https://ui.adsabs.harvard.edu/abs/2020arXiv200508745J

[10] Aprile, E. et al. XENON1T Collaboration. Conceptual design and simulation of a water Cherenkov muon veto for the XENON1T experiment. JINST. astro-ph.IM. **9**, P11006 (2014). doi:10.1088/1748-0221/9/11/P11006

[11] Aprile, E. and others. XENON Collaboration. Projected WIMP sensitivity of the XENONnT dark matter experiment. JCAP. physics.ins-det. doi:10.1088/1475-7516/2020/11/031

[12] Christmann, Mirco and others. MAGIX Collaboration. Light Dark Matter Searches with DarkMESA, PoS, EPS-HEP2021, 129 (2022). doi:10.22323/1.398.0129

[13] Alexander, T. and others. DarkSide search for dark matter. JINST. **8**, C11021(2013). doi:10.1088/1748-0221/8/11/C11021

[14] Pocar, Andrea. EXO-200, nEXO collaboration. Searching for neutrino-less double beta decay with EXO-200 and nEXO. Nucl. Part. Phys. Proc. **42**, 265-266 (2015) doi:10.1016/j.nuclphysbps.2015.06.011

[15] Tosi, D. EXO collaboration. Search for double beta decay with EXO-200. AIP Conf. Proc. **1560**, 187-189 (2013).doi:10.1063/1.4826749

[16] Gornea, Razvan. EXO-200 collaboration. Double beta decay in liquid xenon. J. Phys. Conf. Ser. **179**, 012004 (2009). doi:10.1088/1742-6596/179/1/012004

[17] Birks, John B. The Theory and practice of scintillation counting. (1964). https://www.slac.stanford.edu/spires/find/books

[18] Zhezher, Y. Telescope Array collaboration. Study of Muons in Ultra-High-Energy Cosmic-Ray Air Showers with the Telescope Array Experiment. Phys. Atom. Nucl. **82**, 685-688 (2020) doi:10.1134/S1063778819660517

[19] Erhart, Andreas and others. NUCLEUS collaboration. Development of an Organic Plastic Scintillator based Muon Veto Operating at Sub-Kelvin Temperatures for the NUCLEUS Experiment. 19th International Workshop on Low Temperature Detectors. doi:10.1007/s10909-022-02842-5

[20] Seo, J. W. and Jeon, E. J. et al. A feasibility study of extruded plastic scintillator embedding WLS fiber for AMoRE-II muon veto. Nucl. Instrum. Meth.A. **1039**, 167123 (2022). doi:10.1016/j.nima.2022.167123

[21] K.J. Thomas and E.B. Norman and A.R. Smith and Y.D. Chan. Installation of a muon veto for low background gamma spectroscopy at the LBNL low-background facility. Nuclear Instruments and Methods in Physics Research Section A: Accelerators, Spectrometers, Detectors and Associated Equipment. doi:10.1016/j.nima.2013.05.034

[22] Pla-Dalmau, A. and Bross, A. D. and Mellott, K. L. Low-cost extruded plastic scintillator. Nucl. Instrum. Meth. A. **466**, 482-491 (2001) doi:10.1016/S0168-9002(01)00177-2

[23] Moiseev, A. A. and Hartman, et al. High Efficiency Plastic Scintillator Detector with Wavelength Shifting Fiber Readout for the GLAST Large Area Telescope. Nucl. Instrum. Meth. A. **583**, 372-381 (2007). doi:10.1016/j.nima.2007.09.040

[24] Vaishali Manojkumar Thakur and Amit Jain and others. Design and development of a plastic scintillator based whole body beta/gamma contamination monitoring system. Nuclear Science and Techniques. **32**, 5 (2021). doi:10.1007/s41365-021-00883-1

[25] Holm, U. and Wick, K. Radiation Stability of Plastic Scintillators and Wave Length Shifters. IEEE Trans. Nucl. Sci. **36**, 579-583 (1989). doi:10.1109/23.34504

[26] Bloise, C. and others. Design, assembly and operation of a Cosmic Ray Tagger based on scintillators and SiPMs. Nucl. Instrum. Meth. A. **1045**, 167538 (2023). doi:10.1016/j.nima.2022.167538

[27] Buzhan, P. and Karakash, A. Hand-foot monitors for nuclear plants based on scintillator–WLS–SiPM technology. J. Phys. Conf. Ser. **1689**, 012011 (2020). doi:10.1088/1742-6596/1689/1/012011

[28] Bugg, W. and Efremenko, Yu. and Vasilyev, S. Large Plastic Scintillator Panels with WLS Fiber Readout; Optimization of Components. Nucl. Instrum. Meth. A. **758**, 91-96 (2014). doi:10.1016/j.nima.2014.05.055

[29] Jia-Ning Dong and Yun-Long Zhang and Zhi-Yong Zhang and Dong Liu and Zi-Zong Xu and Xiao-Lian Wang and Shu-Bin Liu. Position-sensitive plastic scintillator detector with WLS-fiber readout. Nuclear Science and Techniques. **29**, 117 (2018)doi:10.1007/s41365-018-0449-2

[30] Y Yang, CP Yang, J Xin, et al. Performance of a plastic scintillation fiber dosimeter based on different photoelectric devices. NUCL SCI TECH. **32**, 120 (2021). https://doi.org/10.1007/s41365-021-00965-0

[31] Adam, T. and others. The OPERA experiment target tracker. Nucl. Instrum. Meth. A. **577**, 523-539 (2007). doi:10.1016/j.nima.2007.04.147

[32] Adamson, P. and others. MINOS collaboration. The MINOS scintillator calorimeter system. IEEE Trans. Nucl. Sci. **49**, 861-863 (2002). doi:10.1109/TNS.2002.1039579

[33] Wang, Ya-Ping and Hou, Chao and Sheng, Xiang-Dong and others. Testing and analysis of the plastic scintillator units for LHAASO-ED. Rad. Det. Tech. Meth. **54**, 513-519 (2021). doi:10.1007/s41605-021-00274-5

[34] Aharonian, F. and others. LHAASO collaboration. Performance test of the electromagnetic particle detectors for the LHAASO experiment. Nucl. Instrum. Meth. A. **1001**, 165193 (2021). doi:10.1016/j.nima.2021.165193

[35] Evans, Justin. MINOS collaboration. The MINOS Experiment: Results and Prospects,Adv. High Energy Phys. **2013**, 182537 (2013). doi:10.1155/2013/182537

[36] Orsi, Silvio. PAMELA collaboration. PAMELA: A payload for antimatter matter exploration and light nuclei astrophysics. Nucl. Instrum. Meth. A. **580**, 880-883 (2007) doi:10.1016/j.nima.2007.06.051

[37] Andreev, V. and others. A high granularity scintillator hadronic-calorimeter with SiPM readout for a linear collider detector. Nucl. Instrum. Meth. A. **540**, 368-380 (2005). doi:10.1016/j.nima.2004.12.002

[38] Thompson, David J. and Wilson-Hodge, Colleen A. Fermi Gamma-ray Space Telescope. arXiv:2210.12875. astro-ph.HE. doi:2210.12875

[39] S. Procureur. Muon imaging: Principles, technologies and applications. Nuclear Instruments and Methods in Physics Research Section A: Accelerators, Spectrometers, Detectors and Associated Equipment. doi:10.1016/j.nima.2017.08.004

[40] Morishima, Kunihiro and others. Discovery of a big void in Khufu's Pyramid by observation of cosmic-ray muons. Nature. **552**, 7685, 386-390 (2017). doi:10.1038/nature24647

[41] Zenoni, Aldo. Historical building stability monitoring by means of a cosmic ray tracking system. 4th International Conference on Advancements in Nuclear Instrumentation Measurement Methods and their Applications. IEEE Nucl.Sci. Symp.Conf.Rec. doi:10.1109/ANIMMA.2015.7465542

[42] Marteau, J. and Gibert, D. et al. Muons tomography applied to geosciences and volcanology. Nucl. Instrum. Meth. A. **695**, 23-28 (2012). doi:10.1016/j.nima.2011.11.061

[43] Oguri, S. and Kuroda, Y. et al. Reactor antineutrino monitoring with a plastic scintillator array as a new safeguards method. Nucl. Instrum. Meth. A. **757**, 33-39 (2014). doi:10.1016/j.nima.2014.04.065

[44] Georgadze, A. Sh. and Pavlovych, V. M.et al. A remote reactor monitoring with plastic scintillation detector. arXiv:1610.05884. doi:/1610/05884/

[45] Scovell, P. R. and others. Low background anti-neutrino monitoring with an innovative composite solid scintillator detector. 2013 IEEE Nuclear Science Symposium and Medical Imaging Conference and Workshop on Room-Temperature Semiconductor Detectors. doi:10.1109/NSSMIC.2013.682954

[46] Capozzi, Francesco and Lisi, Eligio and Marrone, Antonio. Mapping reactor neutrino spectra from TAO to JUNO. Phys. Rev. D. **102**, 056001 (2020). doi:10.1103/PhysRevD.102.056001

[47] S. Agostinelli and others. Geant4—a simulation toolkit. Nuclear Instruments and Methods in Physics Research Section A: Accelerators, Spectrometers, Detectors and Associated Equipment. doi:10.1016/S0168-9002(03)01368-8

[48] Riggi, S. and La Rocca, P. et al. Geant4 simulation of plastic scintillator strips with embedded optical fibers for a prototype of tomographic system. Nucl. Instrum. Meth. A. doi:10.1016/j.nima.2010.10.012

[49] Wenzhen XU and Yanfen LIU and Zongquan TAN and Ran XIAO and Wei KONG and Bangjiao YE. Geant4 simulation of plastic scintillators for a prototype uSR spectrometer. Nuclear Science and Techniques. **24**, 4 (2013) doi:10.13538/j.1001-8042/nst.2013.04.011

[50] Lecoq, P. Scintillation Detectors for Charged Particles and Photons. Particle Physics Reference Library. Springer. Cham, 45-89 (2020). doi:10.1007/978-3-030-35318-6-3

[51] Min Li and Zhi Min Wang and Cai Mei Liu and Pei Zhi Lu and Guang Luo and Yuen Keung Hor and Jin Chang Liu and Chang-Gen Yang. Performance of compact plastic scintillator strips with wavelength shifting fibers using a photomultiplier tube or silicon photomultiplier readout. Nuclear Science and Techniques. **34**, 2 (2023). doi:10.1007/s41365-023-01175-6

[52] Yang, Hang and Luo, Guang. et al. MuGrid: A scintillator detector towards cosmic muon absorption imaging. Nucl. Instrum. Meth. A. **1042**, 167402 (2022). doi:10.1016/j.nima.2022.167402

[53] Hoton Technology Co. Beijing Hoton Nuclear Technology Co., Ltd. doi://www.hoton.com.cn

[54] Tur, Clarisse and Solovyev, Vladimir and Flamanc, Jeremy. Temperature characterization of scintillation detectors using solid-state photomultipliers for radiation monitoring ap-

plications. Nucl. Instrum. Meth. A. **620**, 351-358 (2010). doi:10.1016/j.nima.2010.03.141

[55] Dietz Laursonn, Erik. Detailed Studies of Light Transport in Optical Components of Particle Detectors. Aachen, Tech. Hochsch. doi:inspirehep.net/literature/1505685

[56] Qian, Xiang-Li and Sun, Hui-Ying and Liu, Cheng and Wang, Xu and Martineau-Huynh, Olivier. Simulation study on performance optimization of a prototype scintillation detector for the GRANDProto35 experiment. Nucl. Sci. Tech. **32**, 51 (2021). doi:10.1007/s41365-021-00882-2

[57] Gaisser, Thomas. Cosmic-Ray Showers Reveal Muon Mystery. APS Physics. **9**, 125 (2016). doi:10.1103/Physics.9.125

[58] Shukla, Prashant and Sankrith, Sundaresh. Energy and angular distributions of atmospheric muons at the Earth. Int. J. Mod. Phys. A. **33**, 1850175 (2018). doi:10.1142/S0217751X18501750

[59] Semiconductor Components Industries, LLC. Cherry Semiconductor. (1999-2023). doi:onsemi.com